ANNALS OF GEOPHYSICS, 66, 2, SE208, 2023; doi:10.4401/ag-8848
OPEN ACCESS

# Shear-wave splitting perspectives from the intense aftershock sequence of Damasi – Tyrnavos

George Kaviris*,[1]

(1) Section of Geophysics – Geothermics, Department of Geology and Geoenvironment, National and Kapodistrian University of Athens, Athens, Greece

Article history: received May 29, 2022; accepted September 23, 2022

## Abstract

The area of Damasi – Tyrnavos (Thessaly, Central Greece), in the vicinity of Larissa, was characterized by low seismic activity during the last decades. Two strong earthquakes of Mw = 6.3 and Mw = 6.0 occurred in early March 2021, followed by an intense aftershock sequence, related to WNW-ESE to NW-SE oriented faulting. This sequence was recorded by a dense local seismological network that provided a rich dataset and a unique opportunity to investigate upper crust shear-wave splitting for the first time in the study area. A fully automated technique, employing the eigenvalues method and cluster analysis, was implemented to measure the fast shear-wave polarization direction and the time-delay between the two split-shear-waves. This procedure yielded 655 results of adequate quality grade at 9 stations, after analyzing 1602 events and applying strict selection criteria, including the shear-wave window. The measured directions revealed a complex upper crust anisotropic regime. Anisotropy directions at stations installed at the northern and eastern parts of the study area strike WNW-ESE to NW-SE, in accordance both with the APE model, being parallel to the local $\sigma_{Hmax}$ direction, and the strike of the fault planes. On the other hand, stations at the central part exhibit NNW-SSE and NNE-SSW anisotropy directions. An interesting feature is that the two northern stations are characterized by larger normalized time-delay values, possibly related to the migration of seismicity to the north during the initial stage of the seismic sequence.

Keywords: Seismic anisotropy; Shear-wave splitting; Thessaly; Aftershock sequence; APE

## 1. Introduction

Over half a century has passed since the recognition of seismic anisotropy as a phenomenon that occurs in the Earth's interior [Hess, 1964]. It is described by the variation of seismic velocity at different propagation or polarization directions. The latter is associated with the occurrence of Shear-wave Splitting (SwS). At the source, the shear-wave starts off with the same propagation velocity at all directions. When it enters an anisotropic medium, it splits in two separate shear waves. The $S_{fast}$, travelling at a higher speed and polarized according to the main anisotropic feature, and the $S_{slow}$, polarized orthogonally and traversing the medium with a lower velocity. Two important quantities are commonly used to represent SwS; (a) the polarization direction of the $S_{fast}$ ($\varphi$) and (b) the time-delay between the arrival (or propagation) times of the $S_{fast}$ and the $S_{slow}$ waves ($dt$). As the waveforms are

recorded at a station, the difference in the propagation velocity of the two shear-waves results in an increasing $dt$ as the ray path travelled through the anisotropic medium increases. To account for this effect, $dt$ is commonly normalized by the hypocentral distance, called normalized time-delay ($dt_n$).

The SwS phenomenon is commonly attributed to fabric-related properties of rocks, such as the orientation of olivine crystals in the upper mantle [Ismaïl and Mainprice, 1998; Tommasi et al., 1999; Evangelidis, 2017; Kaviris et al., 2018a]. In the upper crust, one of the primary causes of anisotropy is the existence of fluid-filled microcracks, whose long axes are aligned according to the maximum horizontal compressive stress component $\sigma_{Hmax}$ [Crampin and Zatsepin, 1997; Zatsepin and Crampin, 1997]. The cracks gradually close in this direction under the effect of stress and their aspect ratio is inverted. Thus, values of $\varphi$ are rotated by 90°, when such a flip occurs. Moreover, as stress accumulates and the microcracks expand, the time-delay values also increase, up to the critical point of coalescence (the latter accompanied by a sharp decrease in $dt$). The above processes are described by the Anisotropic Poro-Elasticity (APE) model. Its applicability and implications have been discussed in numerous papers [e.g., Crampin et al., 2013; Kaviris et al., 2015, 2017; Nolte et al., 2017; Crampin and Gao, 2018]. The most important consequence of APE concerns the coalescence stage, which, according to the theory of dilatancy, represents the preparation that precedes an earthquake. Hence, if coalescence could be monitored and identified, we would be able to evaluate the occurrence of an impending major seismic event. Indeed, Crampin et al. [1999] achieved such a "stress-forecast" a couple of weeks before the occurrence of an M = 5.0 event in Iceland – although statistical scrutiny of their forecast did not confirm or reject the hypothesis [Seher and Main, 2004]. APE and its earthquake predicting capabilities have been extensively discussed in the literature, with observations being made in hindsight [Crampin, 2001; Gao and Crampin, 2006; Crampin et al., 2008, 2015; Polat et al., 2012; Kaviris et al., 2018b]. Anisotropy could also be attributed to the existence of local structures which lead to microcrack orientations different than the one of the regional stress field [Kaneshima et al., 1988; Kaneshima, 1990]. Structurally-controlled anisotropy has been identified in various cases, with $\varphi$ differing from the orientation of $\sigma_{Hmax}$ and being aligned to local structures [Zinke and Zoback, 2000; Balfour et al., 2005; Boness and Zoback, 2006; Li et al., 2014; Li and Peng, 2017; Pastori et al., 2019; Kaviris et al., 2021]. It is evident that in areas where tectonic structures and $\sigma_{Hmax}$ align, it is difficult to distinguish between stress-induced and structurally-controlled anisotropy. This could limit the potential of SwS as a stress-monitoring and, therefore, earthquake forecasting tool.

Larissa city and Tyrnavos town are located in Thessaly, Greece. Thessaly has suffered several damaging and destructive events [Ambraseys and Jackson, 1990; Papadimitriou and Karakostas, 2003; Papazachos and Papazachou, 2003; Stucchi et al., 2013]. Nonetheless, the majority has occurred away from Larissa and Tyrnavos. Caputo and Helly [2005] present a series of evidence from paleoseismic, archaeological and historical proof for strong and destructive earthquakes in the area. They mention three additional strong events at Larissa (7$^{th}$ to 15$^{th}$ century BCE, 1731 and 1941 CE), as well as one near the present-day location of Tyrnavos, which occurred 5.3 to 6.9 ka BCE, with an estimated magnitude between 6.0 and 6.5. Moreover, they mention that the area is dominated by ESE-WNW-trending normal dip-slip faults of lengths over 10 km [Caputo et al., 2004].

During the recent decades of network densification (after the 1980s), the region around Larissa and Tyrnavos did not host any intense seismic sequences [Makropoulos et al., 2012]. In March 2021, this situation changed. A strong Mw = 6.3 earthquake occurred on March 3$^{rd}$, 2021, and was followed by another strong Mw = 6.0 event (Figure 1) on March 4$^{th}$, 2021 [Karakostas et al., 2021; Koukouvelas et al., 2021; Lekkas et al., 2021; Mavroulis et al., 2021; Papadopoulos et al., 2021; Kassaras et al., 2022; Michas et al., 2022]. The mainshock and its aftershocks caused observable ground deformations [De Novellis et al., 2021; Tolomei et al., 2021; Song et al., 2022; Yang et al., 2022] and thermal anomalies [Kouli et al., 2021]. The direction of extension determined for the 2021 sequence was reported to be different than the known stress regime in the area [Galanakis et al., 2021; Lazos et al., 2021]. Swiftly organized campaigns by the Aristotle University of Thessaloniki (AUTH) and the University of Patras (UPAT) installed sensors at 10 sites to monitor the area. The rich aftershock sequence (over 3500 earthquakes) revealed the activation of WNW-ESE to NW-SE structures. This orientation is also imprinted in other characteristics of the sequence; the extension of epicenters along a well-defined 50 km-long NW-SE area (Figure 1), in patches loaded by the occurrence of the larger events [Kassaras et al., 2022]. Even though surficial phenomena (e.g., liquefactions and soil fissures) were observed [Valkaniotis et al. 2021; Papathanassiou et al., 2022], the earthquakes have been attributed to a blind fault [Chatzipetros et al., 2021; Pavlides and Sboras, 2021]. The wealth of data sparked new interest in the area, with several aspects of the sequence having been studied, such as accelerating deformation seismicity patterns [Chatzopoulos, 2021] and earthquake early warning [Spingos et al., 2021].

In the framework of the present work, an upper crust seismic anisotropy study was conducted for the first time in Thessaly, at the Damasi – Tyrnavos area, where the intense 2021 seismic sequence occurred. The utilized data were recorded by stations belonging to the Hellenic Unified Seismic Network (HUSN) and, mainly, by temporary stations installed to monitor the sequence. Shear-wave splitting results were obtained using a fully automated method through the Pytheas software (Spingos et al., 2020). Temporal variations of the time-delays were also examined, to investigate any possible relation with occurrences of significant events.

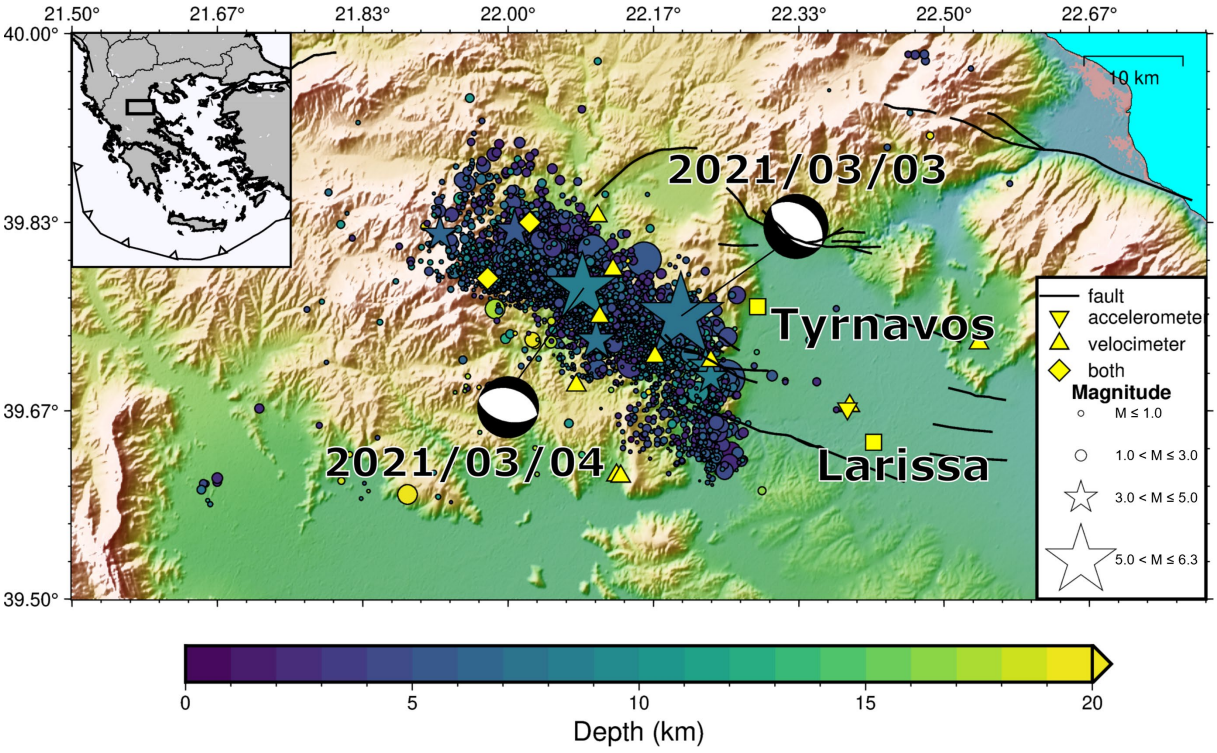


**Figure 1.** Seismotectonic map of the March 2021 sequence in Thessaly. Epicenters (circles) form a roughly NW-SE-oriented aftershock area. The largest events ($M \geq 5.0$) are shown (stars). Earthquake symbols are color-coded according to their respective focal depth. The sequence was closely monitored by permanent and temporary seismographs (triangles), an accelerometer (inverted triangle) and sites equipped with both types of sensors (diamonds). Beachballs for focal mechanisms of the two largest events are also shown, adopted from Ganas et al. [2021] and Kassaras et al. [2022]. Tyrnavos and Larissa are depicted as squares. Faults (black lines) are from the NOAfaults v4.0 database [Ganas et al., 2017; Ganas, 2022].

## 2. Data Selection and Shear-wave Splitting Processing

A total of 1630 earthquake locations were acquired from the manually revised bulletin of the Seismological Laboratory of the National and Kapodistrian University of Athens (SL-NKUA). The catalog starts from June 2018 (the beginning of the publicly available bulletin) and lasts until July 2021. Given that the strong earthquakes of the sequence occurred in March, the selected duration covers about five (5) months of activity. Moreover, only events with magnitudes $M_L \geq 2.0$ were included. Lowering the threshold to include all detected events (minimum $M_L$ of 0.2) would lead to a catalog of 3971 earthquakes, for the same area and time period. The selected sample of over 1500 locations is more than adequate to investigate the state of splitting in Thessaly, as processing events with clearer and more impulsive shear-wave arrivals due to their higher energy content was assured. The final catalog has an average Root Mean Square (RMS) origin error of 0.52 s, with average spatial uncertainties corresponding to 1.3 km and 1.4 km, for the horizontal and vertical planes, respectively. Depths of the vast majority of the events are constrained to the uppermost 10 km of the crust, with the mean being 6.2 km. The average magnitude (excluding the two main events) is 2.4.

Waveform data were acquired from the European Integrated Data Archive (EIDA) node at GI-NOA [Evangelidis et al., 2021]. Before the 2021 seismic crisis, the Larissa – Damasi – Tyrnavos area was locally monitored by three permanent seismological stations, belonging to the Geodynamic Institute of the National Observatory of Athens (GI-NOA) (HL; https://doi.org/10.7914/SN/HL) [National Observatory Of Athens, Institute of Geodynamics, 1997] and AUTH (HT; https://doi.org/10.7914/SN/HT) [Aristotle University of Thessaloniki Seismological Network, 1981]; seismometers at Larissa (HL.LRSO) and Tyrnavos (HT.TYRN) and an accelerometer in the outskirts of Larissa (HL.GINA). After the occurrence of the first strong event of March, AUTH installed seven temporary broadband sensors and the University of Patras (HP; https://doi.org/10.7914/SN/HP) [University of Patras, Geology Department, 2000] two additional ones. All data streams were set at a sampling rate of 100 samples/sec. From that point on, the aftershock sequence was being closely monitored. Data and metadata retrieval, as well as preprocessing (removal of signal trend and mean) were performed with ObsPy [Krischer et al., 2015; Beyreuther et al., 2010]. Concerning phase arrivals, the manually determined ones were acquired from the bulletin of SL-NKUA.

The shear-wave window criterion was applied to avoid recordings of direct and secondary shear-wave co-arrivals, which could lead to erroneous identification or measurement of the SwS parameters. This window refers to rays within a range of angles of incidence (starting from vertical 0°), $i_h$, which is commonly used in shear-wave splitting studies. The upper limit of this window was initially proposed as $i_h^{max} = \sin^{-1}\frac{V_s}{V_p}$, considering the P- ($V_p$) and S- ($V_s$) velocities at the uppermost layer (Evans, 1984) and typically having values of ~35°. Nevertheless, it was later shown that for curved wavefronts, a thin surficial layer of low velocity (e.g. comprised of sediments) can distort the ray path towards the vertical plane and permits a wider shear-wave window of 45°. This increase enables the extension of the dataset. In the Damasi – Tyrnavos case, the formulation of Evans [1984] yielded a maximum incidence angle of 35.4°, derived from a $V_p/V_s$ of 1.73 for the topmost layer [Kassaras et al., 2022]. Ray paths for all arrivals included in the catalog of SL-NKUA were calculated with TauP [Crotwell et al., 1999] and the 1-D velocity model of Kassaras et al. [2022]. A total of 2705 initial S-arrivals were found within the extended shear-wave window, with only 30 emerging at angles between 35° and 45°. It is noted that in today's landscape of large datasets, discarding potentially unsuitable event-station pairs saves valuable processing resources and time. Finally, the application of the shear-wave window criterion reduced the number of suitable events to 891.

Shear-wave splitting analysis was conducted using the Pytheas software (Spingos et al., 2020). This suite offers multiple options for analysis, including manual evaluation through polarigrams and particle motion diagrams [Bernard and Zollo, 1989; Papadimitriou et al., 1999; Kaviris, 2003; Kaviris et al., 2017, 2018c], semi-automatic processing [Bowman and Ando, 1987; Silver and Chan, 1991] and fully automated procedures [Teanby et al., 2004; Savage et al., 2010]. In the present study, the method of Eigenvalues (EV) automated with the aid of Cluster Analysis (CA) was preferred [Silver and Chan, 1991; Teanby et al., 2004]. First, the program performs a check for each event-station pair. If it does not meet two fundamental conditions – i.e., having an angle of incidence less than or equal to 45° and a Signal-to-Noise Ratio (SNR) of at least 1.5 – it is skipped. The first condition was true for all pairs in the final catalog, given that this check was performed in the preparation stage, as mentioned previously. To remove noise from the signal, a bandpass filter was applied. However, instead of predefining a single bandwidth, various trial corner frequencies were tested to find the one that provides the clearest signal [Savage et al., 2010]. Next, Pytheas grossly estimates the frequency of shear-waves in a predefined time window around their catalog-provided arrival-time.

After taking these preparatory steps, the software defines a range of time windows around the arrival, considering the S-P arrival time difference (for the furthest window beginning) and the evaluated shear-wave period (for the furthest window ending). For each signal window, the EV method of Silver and Chan [1991] is applied. For a combination of trial $\varphi$ and $dt$ pairs (ranging from N0°E to N179°E and from 0.0 to 300.0 ms, respectively), the following procedure is used. First, horizontal waveforms are rotated according to the trial $\varphi$ value (i.e., rotated to a co-ordinate system defined by the fast and slow shear-wave polarizations). The component now corresponding to the slow arrival is temporally shifted by the trial $dt$ value towards the arrival of the $S_{fast}$. Then, the waveforms are rotated back to their initial axial system. The covariance matrix of the two horizontal components is calculated and its second (minimum) eigenvalue ($\lambda_2$) is obtained. It is noted that the initial axial system of the waveforms is the one defined by the ray path. According to Silver and Chan [1991], in the absence of anisotropy and noise, the shear-wave energy should be null for SKS phases in the transverse component. Nevertheless, in real-world conditions it is impossible to completely remove noise or the splitting effect. Therefore, out of an array of $\varphi$ and $dt$ combinations, the minimum $\lambda_2$ should correspond to the pair that best removes anisotropy. The original proposal of Silver and

Chan (1991) contained a statistical framework for estimating the uncertainties of the two splitting parameters. However, Walsh et al. [2013] found that the initial formulations could underestimate the errors and proposed new ones. Pytheas incorporates the latter.

As described above, the software yields a set of splitting parameters for each candidate signal window, forming a space described by $\varphi$ and $dt$. Teanby et al. [2004] proposed an automatic solution to search for the stabler splitting measurement by forming clusters. Pytheas adopts this scheme. Thus, after EV is performed in all windows, observations are cumulatively hierarchically clustered and the number of clusters is automatically selected. The measurement with the smallest error from the most constrained cluster is considered as the final result, yielding the values of $\varphi$ and $dt$ for each event-station pair.

Moreover, the automatic grading solution of the software was used. In the above procedure, the cross-correlation coefficient between the waveforms in the fast-slow and north-east axial systems is obtained, after correcting for anisotropy. This aims to imitate human visual inspection. If splitting is removed, shear-waves should arrive simultaneously in both horizontal components and have a strong positive or negative correlation. These two coefficients are co-evaluated with the $\varphi$ and $dt$ uncertainties to offer a score for each measurement. Then, the score

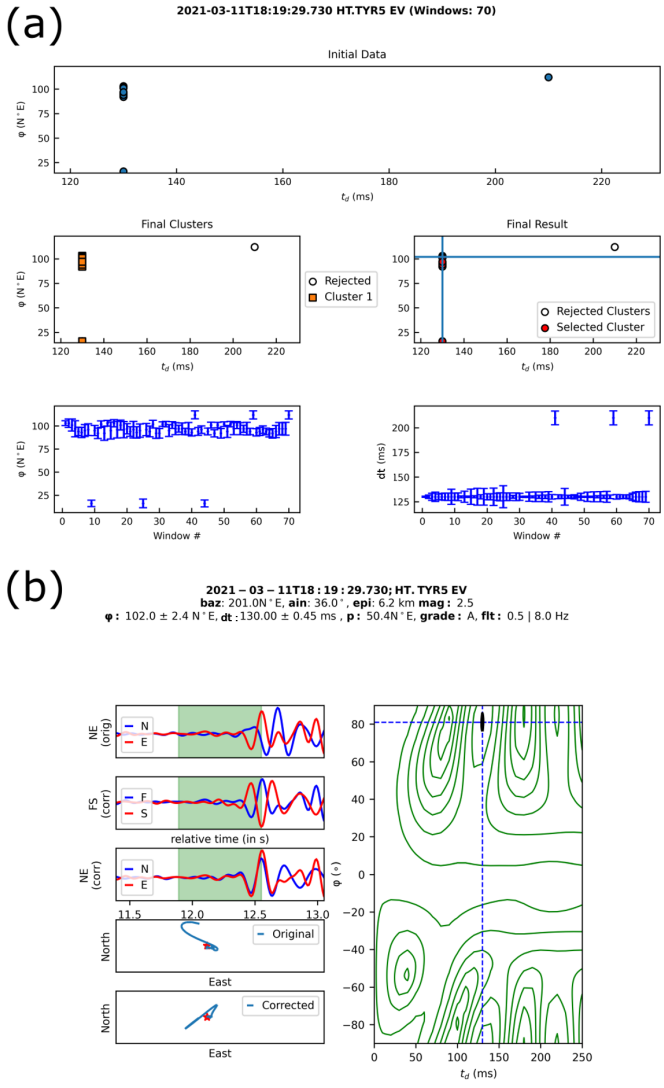


**Figure 2.** Processing example for an event-station pair graded "A". Panel (a) showcases the results of the clustering algorithm, with the initial observation space (top), the formed clusters (middle left) and the selected cluster (middle right) and the variation of both $\varphi$ (bottom left) and $dt$ (bottom right) with the signal window. Panel (b) shows the EV measurement in the optimal signal window. The waveforms of the horizontal channels (top left) and corresponding particle motion diagrams (bottom left), as well as the contour plot of $\lambda_2$ (right) are demonstrated. The bold black contour denotes the 95% confidence interval and the crosshairs indicate the selected solution.

is classified to a quantitative grade (with "A" being best and "E" worst), according to user-defined limits. Finally, observations with similar $\varphi$ and shear-wave polarizations (fast or slow) after the splitting correction ($p$) i.e., when the wave propagates through an isotropic medium or if the initial polarization coincides with either the fast or the slow axis, are considered to be null measurements (Wüstefeld and Bokelmann, 2007) and are discarded.

The example in Figure 2 showcases a summary of the processing scheme. It concerns an earthquake that occurred on 2021-03-11T18:19:29.730 UTC with a magnitude of $M_L = 2.5$ and a depth of 2.3 km. The epicenter was located at a distance of 6.2 km from station HT.TYR5, one of the temporary broadband stations installed by AUTH, at a backazimuth of N201°E. The ray was estimated to leave the source at a takeoff angle of 87° and emerge at the surface 36° from the vertical plane. This example denotes the importance of adopting a wider shear-wave window, when conditions permit it. Even though the ray has an angle of incidence just above the calculated 35° window, it would have been de facto rejected if the window was not extended to 45°. As seen in Figure 2a, 70 signal windows were considered. However, measurements are rather stable and, visually, one cluster can be identified, which is also confirmed by the algorithm. According to Figure 2a, 67 of the measurements indicate a $\varphi$ value around N100°E and $dt$ around 130 ms. It is noted that no other clusters were identified because the software has been parameterized to only form clusters with over 5 samples. In Figure 2b, the EV measurement over the selected signal window is shown. The window correctly includes the first shear-wave arrivals on both horizontal components. The corrected waveforms showcase the high similarity of shear-wave arrivals, which can now be considered simultaneous. The polarization direction of the $S_{fast}$ was found to be N102°E and the time-delay was equal to 130 ms. The polarization of the corrected shear-wave was N50°E, neither parallel nor perpendicular to $\varphi$, meaning that it is not a null observation. The small errors (~2° for $\varphi$ and ~0.5 ms for $dt$) and the high cross-correlation coefficients for the corrected waveforms (0.97 for both the fast-slow and north-east axial systems) led the grading algorithm to assign a grade of "A".

## 3. Results

The processing scheme produced 1668 splitting observations, out of which 1006 were graded as "E", 7 as "D", 132 as "C", 375 as "B" and 148 as "A". These results were obtained for 9 stations. After considering only the ones graded "A", "B" or "C" as suitable, the final dataset comprised 655 parameter pairs. Results are summarized in Table 1. The average direction of the fast polarization direction and its error were calculated with circular statistics [Berens, 2009]. The time-delay normalized per the hypocentral distance ($dt_n$) is also presented. Individual errors for $dt_n$ were obtained using the formula proposed by del Pezzo et al. [2004].

| Station Code | N | $\bar{\varphi}$ (N°E) | $\delta\bar{\varphi}$ (°) | $\overline{dt}$ (ms) | $\overline{dt_n}$ (ms) | $\delta\overline{dt}$ (ms/km) | $\delta\overline{dt_n}$ (ms/km) |
|---|---|---|---|---|---|---|---|
| All | 655 | 131.5 | 0.5 | 89 | 2 | 8.3 | 0.2 |
| HP.KANL | 83 | 88.1 | 5.7 | 99 | 5 | 10.3 | 0.7 |
| HP.VRKS | 69 | 105.8 | 4.7 | 79 | 5 | 7.3 | 0.5 |
| HT.TYR1 | 82 | 8.6 | 1.0 | 85 | 6 | 7.5 | 0.6 |
| HT.TYR2A | 17 | 119.8 | 24.6 | 95 | 13 | 7.1 | 1.2 |
| HT.TYR3 | 62 | 25.6 | 1.0 | 80 | 9 | 7.2 | 0.7 |
| HT.TYR4 | 93 | 130.2 | 1.0 | 72 | 5 | 7.1 | 0.5 |
| HT.TYR5 | 85 | 103.8 | 23.1 | 116 | 6 | 11.2 | 0.7 |
| HT.TYR6 | 69 | 168.0 | 0.7 | 94 | 7 | 7.4 | 0.6 |
| HT.TYRN | 95 | 160.6 | 0.9 | 84 | 7 | 7.8 | 0.7 |

**Table 1.** Average splitting parameters for all stations and per station, with their respective standard error of the mean (δ), along with the respective number of observations ($N$).

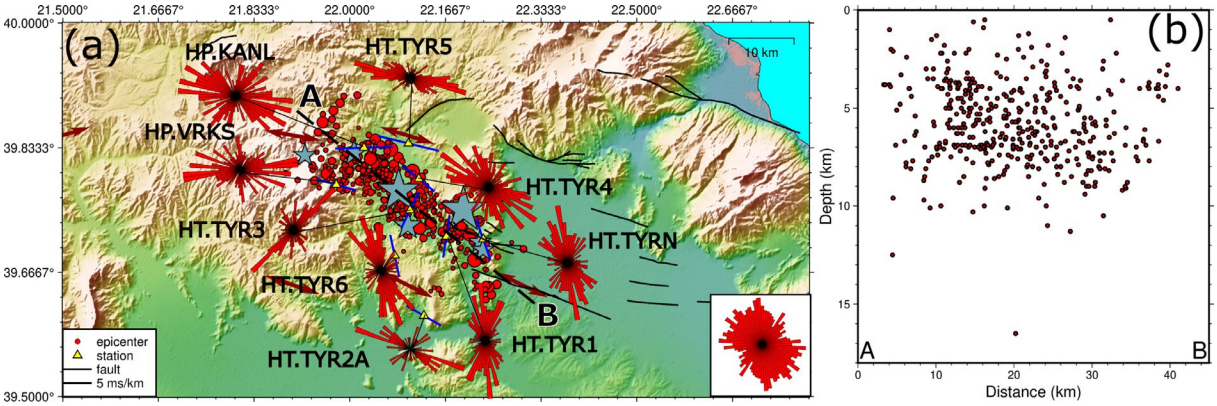


**Figure 3.** (a) Map of earthquakes represented in the final dataset (circles) and significant events with M ≥ 5.0 (stars). At each station (yellow triangles), the vector that denotes the average $\varphi$ and $dt_n$ of Table 1 is drawn (blue vectors). Rose diagrams for each station are presented, along with the rose diagram of all measurements in the bottom right corner. The double-headed arrows note the $\sigma_{Hmax}$, as given by Kassaras et al. [2022]. Faults (black lines) are after Ganas et al. [2017]. Earthquake symbols are scaled according to their magnitude, as in Figure 1. The profile line A-B on the map is used for the cross-section of Fig. 3b. (b) Cross-section of the hypocenters that yielded shear-wave splitting results along the A-B profile of Fig. 3a.

The average polarization direction from all measurements is N131.5°E, but this is not representative. As seen in the rose diagrams (Figure 3a), a wide variety of $\varphi$ directions can be observed. Two very broad groups can be identified; one around the NNW-SSE direction and one spread around WNW-ESE. Nevertheless, when individual stations are considered, certain spatial patterns are evident. Specifically, the northern stations (HP.KANL, HP.VRKS, HT.TYR4 and HT.TYR5) present average $\varphi$ values indicating a direction around WNW-ESE to NW-SE. It should be noted that station HT.TYRN has a wider spread of $\varphi$ values, with a roughly dominant NNW-SSE direction. The southernmost station (HT.TYR2A) showcases a WNW-ESE main direction, while a distinct NNW-SSE direction in HT.TYR6 is evident. HT.TYR1 is the only station with a very clear NNE-SSW dominant orientation. A general NE-SW direction can be considered for HT.TYR3, although (with the exception of E-W directions) all $\varphi$ groups are represented.

The highest average time-delays are observed in the northernmost stations, i.e. HP.KANL (99 ms) and HT.TYR5 (116 ms). The lowest time-delay (72 ms) is measured at station HT.TYR4, which is located very close to the epicenter of the second M ≥ 6.0 earthquake. The possibility that the highest time delay values at stations HP.KANL and HT.TYR5 may be related to deeper earthquake foci was investigated. However, the hypocenters located close to these stations (towards the point A) that yielded reliable SwS results are not located deeper than the other events that were used in the present study (Figure 3b). In addition, according to Kassaras et al. [2022] who relocated the Damasi – Tyrnavos sequence, the depths of most events are between 6 km and 10 km, including those located at the northern part, close to point A of Figure 3b. Only the aftershocks of the southernmost part of the sequence (close to point B of Figure 3b) were relocated at shallower depths, between 4 km and 8 km. In order to further examine a possible link between the seismicity depth and the observed spatial differences in the time-delays, the relation between $dt$ and depth was examined for each station separately, with the vast majority of the stations (7 out of 9) presenting weak negative correlation. Normalized time-delays are well-constrained in the 7.1 to 7.8 ms/km range, with the exception of stations HP.KANL (10.3 ms/km) and HT.TYR5 (11.2 ms/km). As stated above, these two instruments were installed at the northern edge of the sequence. Other than this distinction, time-delays do not seem to follow a spatial pattern.

## 4. Discussion

The polarization of the fast shear-wave is commonly associated with the existence of preferentially aligned microcracks in the upper layers of the crust [Crampin and Atkinson, 1985]. The alignment is attributed to the regional stress field, which dictates the orientation, as the long axis of the microcracks is oriented according to the maximum horizontal compressive [Cochran et al., 2003, 2006; Ortega-Romo et al., 2021] stress component

($\sigma_{Hmax}$). When a critical threshold of stress accumulation is exceeded, the aspect-ratio of the microcracks is inverted, rotating the fast shear-wave direction by approximately 90°, the so-called "90°-flip". Such interactions have been described by the Anisotropic Poro-Elasticity (APE) model [Crampin and Zatsepin, 1997; Zatsepin and Crampin, 1997]. Nevertheless, deviations from this model are common, with high $\varphi$ scattering being attributed to topographic irregularities [Tai et al., 2011], complex tectonics and structures [Kaviris et al., 2021], fluid pathways [Kaviris et al., 2020] and inherent rock fabric [Valcke et al., 2006]. The control of structures over splitting features is also common in interpreting shear-wave splitting, either as the sole cause or by assessing its interplay with the regional stress field [Cochran et al., 2003, 2006; Peng and Ben-Zion, 2004; Gao et al., 2019; Kaviris et al., 2021; Ortega-Romo et al., 2021].

In the case of the Damasi – Tyrnavos area, $\sigma_{Hmax}$ has been estimated to be oriented generally WNW-ESE, with local tectonics indicating normal faulting in WNW-ESE to NW-SE azimuths [Kapetanidis and Kassaras, 2019; Kassaras et al., 2022]. The aftershock sequence occurred in the mountainous region to the NW of Larissa and its surrounding plain (Figure 1), and it extended in a NW-SE geometry. Therefore, topography could affect $\varphi$ and result to high scattering in the observations. The majority of stations that monitored the aftershock sequence were located in this area of high relief and present high scatter of $\varphi$. However, a general trend of WNW-ESE to NW-SE primary orientations can be identified in all sites, except three. Namely, HT.TYR1 exhibits a well-documented NNE-SSW prevalence and HT.TYR3 a general NE-SW orientation, contrasted by the NNW-SSE direction at HT.TYR6. Therefore, it can be stated that $\varphi$ follows the regional stress field, which is also represented by the similarly oriented major local faults (with the exception of smaller ones having different strikes). The northern and eastern edges of the aftershock area indicate polarization directions in agreement with the stress field. The instruments located in the central part of the area exhibit dominant polarization directions that range between NNW-SSE and NNE-SSW. From the above, two families of microcracks can be identified; one that surrounds the aftershock region and features cracks aligned to $\sigma_{Hmax}$ and one in the center with approximately perpendicular directions.

Another interesting observation concerns the significant increase of average time-delays to the north (stations HP.KANL and HT.TYR5), a result that is not related with the depth of the earthquake foci. With the exception of these two sites, the mean values of the normalized time-delays are close to an average of 7.3 ms/km. It is worth

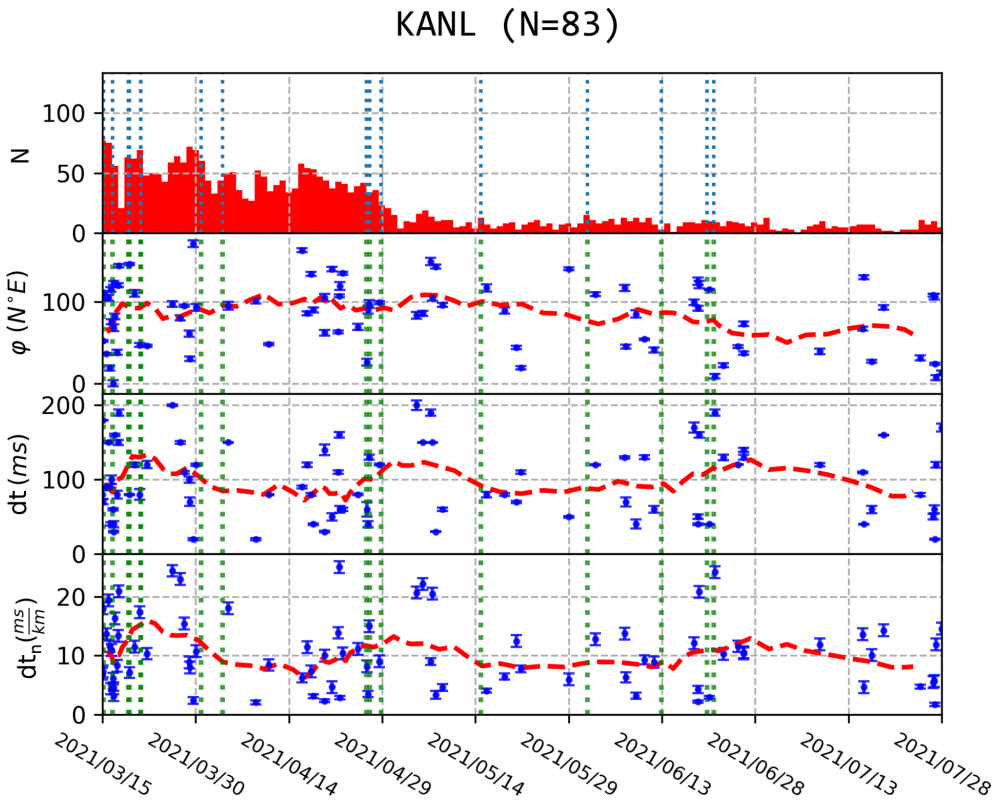


**Figure 4.** (From top to bottom) Histogram of daily seismicity and temporal variations of $\varphi$, $dt$ and $dt_n$ at station HP.KANL. The red dashed line shows the 9-point average. Green dashed lines correspond to the occurrence of events with M ≥ 3.5.

noting that the two northernmost stations average a normalized time-delay of 10.7 ms/km, which signifies a 46% increase. Moreover, it is known that the general evolution of the aftershock sequence was northward [Kassaras et al., 2022]. The question is if stress redistribution from the start of the sequence could have loaded the rock volume closer to these stations and, consequently, increase the aspect ratio of microcracks and affect $dt_n$. To examine this hypothesis, two conditions must be met. The increase should be documented spatially (as shown already) and temporally. Nevertheless, even though the response of both UPAT and AUTH was rapid, there is a significant gap between the occurrence of the two events of March 3rd and 4th, 2021 and available data. In the final dataset, the first observation at HP.KANL is on March 15th, while splitting observations at HT.TYR5 start on March 9th, 2021. Thus, the initial stage of time-delays in the northern edge is unknown. Normalized time-delays in HP.KANL show increase patterns that do not coincide with any $M \geq 3.5$ event (Figure 4). At the end of April, three $3.5 \leq M \leq 4.0$ events occurred, during a period of $dt_n$ increase. However, the increase continued through to May. Therefore, these events cannot be associated with the temporal variations of time-delays. There are no other events of $M \geq 3.5$ that could be linked to any observed variations. Moreover, $dt_n$ does not seem to decrease or increase – on average – as time passes. There is a definite reduction of $dt_n$ values after the first period (March 15th to 30th, 2021). After the abovementioned late April increase, the average $dt_n$ value is generally stable and exhibits no significant trends.

The observation period in HT.TYR5 lasts between March 9th and April 29th, 2021. This is a shorter period than the one documented by HP.KANL, but includes a larger portion of seismicity from the early days of the sequence (March 9th to 15th, 2021). Again, no earthquake-specific (for $M \geq 3.5$) connections can be identified. Nevertheless, normalized time-delays are higher before March 24th, 2021. Then, $dt_n$ decreases and an increase period seems to exist for the later part of the dataset (Figure 5), up to April 29th, 2021. On the last day of observations, an $M_L = 3.6$ event occurred ~15 km SE of the station (~5 km west of HT.TYRN). There are no strong events after this period, that could explain the steady increase in $dt_n$ observed at the station. Moreover, even though there is an increasing trend, independent values do not exceed 20 ms/km; during March, quite a few observations were over that limit. It is noted that there are no significant changes in $\varphi$ during this period. The rest of the stations did not show any significant change in $dt_n$.

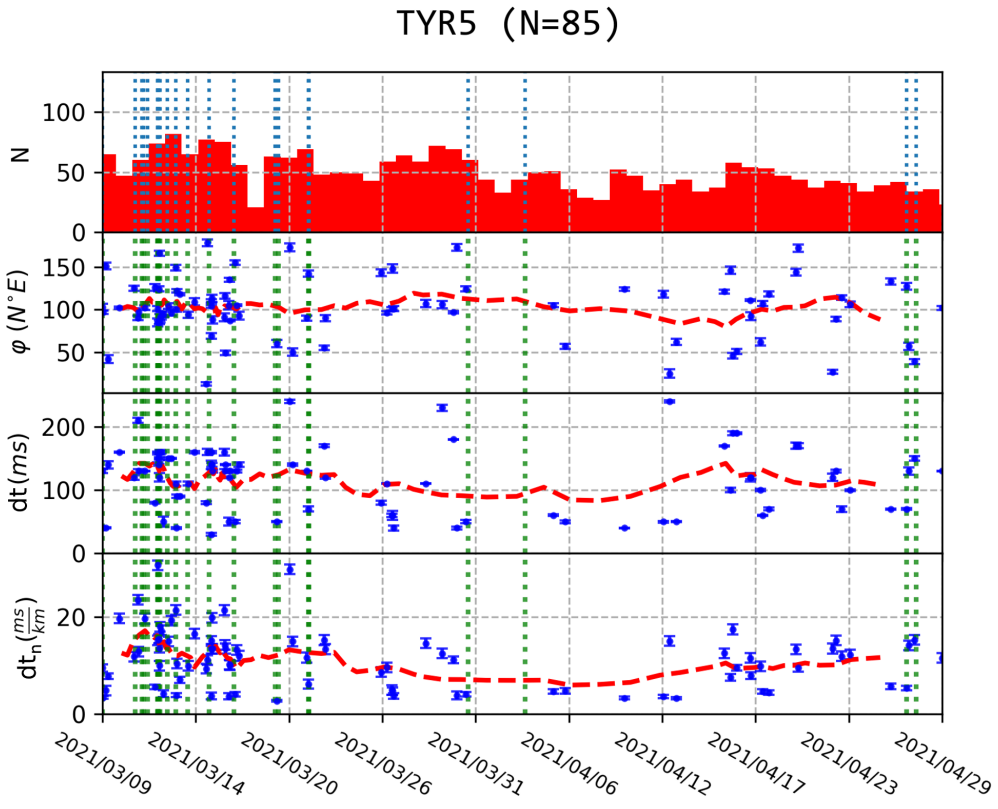


**Figure 5.** (From top to bottom) Histogram of daily seismicity and temporal variations of $\varphi$, $dt$ and $dt_n$ at station HT.TYR5. The red dashed line shows the 9-point average. Green dashed lines correspond to the occurrence of events with $M \geq 3.5$.

The above observations provide a complex picture of splitting in the aftershock area of the Tyrnavos sequence. Unfortunately, only HT.TYRN, being a permanent station, was active before the occurrence of the March 3rd, 2021 mainshock and analysis yielded only 6 results between August 5th, 2019 and November 16th, 2020, while there are no observations between November 17th, 2020 and March 3rd, 2021. Thus, it is impossible to search for temporal variations of the shear-wave splitting parameters before the occurrence of the early March 2021 main events. Assuming the existence of crustal microcracks, the seemingly random behavior of time-delays during the aftershock sequence indicates that either the crack systems are not sensitive to stress variations or that stress redistribution associated with the sequence does not affect the rock volume in such a significant way that also affects time-delays, with the possible exception of the spatial increase of $dt_n$ values towards the north. The complex state of $\varphi$, with possibly two regimes, in this relatively small area (approximately 30 km x 5 km), offers evidence for a multifaceted anisotropic crust. Additionally, the sharp topography affects the recorded shear-waves and could also influence the measured time-delay values. These two elements could obfuscate the true variation of stress, as expressed by the time-delays.

## 5. Conclusions

Crustal anisotropy in the region of Thessaly, Greece, had not been previously explored. Over 1000 recordings of 3-component broadband stations installed in the context of the 2021 Damasi – Tyrnavos sequence were utilized in the framework of this study. Between March 3rd and July 30th, 2021, 3839 events of magnitude over 0.2 occurred, with the main shock of Mw = 6.3 being followed by an Mw = 6.0 earthquake, one day later. Considering that between June 1st, 2018 and the initiation of the sequence only 133 event locations were available in the catalog of SL-NKUA (with only 1 station, HT.TYRN, located relatively close) it was not feasible to investigate the state of the upper crust seismic anisotropy before the March 3rd, 2021 mainshock. The Damasi – Tyrnavos crisis was exploited, by using 1602 detected events and 9 broadband sensors (8 out of which were installed to monitor the sequence, by AUTH and UPAT). Automatic processing produced a dataset comprising 655 shear-wave splitting parameter pairs of good quality, using rays within the shear-wave window (incidence angle $\leq 45°$).

The present work revealed the existence of a complex anisotropic upper crust in Thessaly, in the Damasi – Tyrnavos area. Measurements at stations to the northern and eastern edges of the oval-shaped NW-SE-epicentral area, defined by the 2021 seismic sequence, yielded WNW-ESE to NW-SE dominant fast shear-wave polarization directions, approximately parallel to the maximum horizontal compressive stress component and to the strike of the fault planes of the major events, as determined by focal mechanisms and INSAR/GNSS models [Ganas et al., 2021; Kassaras et al., 2022]. Stations located at the center of the sequence offer wider variety, with the prevalence of NNW-SSE and NNE-SSW polarizations. Spatial dependence of anisotropy can also be identified in some cases. The two northernmost stations (HP.KANL and HT.TYR5) present normalized time-delay values ~46% higher than the rest of the stations, coinciding with the initial northward migration of seismicity. No significant temporal dependence of splitting parameters was observed in any of the stations.

**Acknowledgements.** The author would like to thank the two anonymous reviewers and the handling Editor Dr. L. Margheriti for the constructive and detailed comments that contributed to the improvement of the manuscript. The author thanks the personnel of all cooperating institutes of HUSN for the operation of the stations. The present study is co-funded by the Special Account for Research Grants (S.A.R.G.) of the National and Kapodistrian University of Athens.

**Data and sharing resources.** Waveform data were retrieved from the EIDA node at GI-NOA (http://eida.gein.noa.gr/). The earthquake catalog of SL-NKUA is available online at http://www.geophysics.geol.uoa.gr/stations/gmapv3_db/index.php?lang=en.

The shear-wave splitting analysis was performed with the Pytheas software (https://github.com/ispingos/pytheas-splitting). Circular statistics were computed with pycircstat (https://github.com/circstat/pycircstat).

Maps shown in Figure 1 and 3 were drawn with the Generic Mapping Tools, v.6.0, package [Wessel et al., 2019] and its Python wrapper, PyGMT [Uieda et al., 2021]. Plots used in Figure 2 were produced by Pytheas. Figures 4 and 5 were plotted with Matplotlib [Hunter, 2007].

## References


Aristotle University of Thessaloniki Seismological Network (1981). Permanent regional seismological network operated by the Aristotle University of Thessaloniki, International Federation of Digital Seismograph Networks, https://doi.org/10.7914/SN/HT.

Ambraseys, N. N. and J. A. Jackson (1990). Seismicity and associated strain of central Greece between 1890 and 1988, Geophys. J. Int., 101(3), 663–708, https://doi.org/10.1111/j.1365-246X.1990.tb05577.x

Balfour, N. J., M. K. Savage and J. Townend (2005). Stress and crustal anisotropy in Marlborough, New Zealand: evidence for low fault strength and structure-controlled anisotropy, Geophys. J. Int, 163, 1073–1086, https://doi.org/10.1111/j.1365-246X.2005.02783.x

Berens, P. (2009). CircStat: a MATLAB toolbox for circular statistics, J. Stat. Softw., 31, 10, http://onlinelibrary.wiley.com/doi/10.1002/wics.10/full

Bernard, P., and A. Zollo (1989). Inversion of near-source S polarization for parameters of double-couple point sources, Bull. Seismol. Soc. Am., 79(6), 1779–1809.

Beyreuther, M., R. Barsch, L. Krischer, T. Megies, Y. Behr and J. Wassermann (2010). ObsPy: A Python Toolbox for Seismology, Seismol. Res. Lett., 81(3), 530–533. http://srl.geoscienceworld.org/content/81/3/530.abstract

Boness, N. L. and M. D. Zoback (2006). Mapping stress and structurally controlled crustal shear velocity anisotropy in California, Geology, https://doi.org/10.1130/G22309.1

Bowman, J. and M. Ando (1987). Shear-wave splitting in the upper-mantle wedge above the Tonga subduction zone, Geophys. J. Int., 25–41. http://gji.oxfordjournals.org/content/88/1/25.short

Caputo, R. and B. Helly (2005). Archaeological evidences of past earthquakes: A contribution to the SHA of Thessaly, Central Greece, J. Earthq. Eng., 9, 2, 199–222. https://doi.org/10.1080/13632460509350539

Caputo, R., B. Helly, S. Pavlides and G. Papadopoulos (2004). Palaeoseismological investigation of the Tyrnavos Fault (Thessaly, Central Greece), Tectonophysics, 394(1–2), 1–20. https://doi.org/10.1016/J.TECTO.2004.07.047

Chatzipetros, A., S. Pavlides, M. Foumelis, S. Sboras, D. Galanakis, C. Pikridas, S. Bitharis, E. Kremastas, A. Chatziioannou and I. Papaioannou (2021). The northern Thessaly strong earthquakes of March 3 and 4, 2021, and their neotectonic setting, Bull. Geol. Soc. Greece, 58, 0, 222–255, https://doi.org/10.12681/bgsg.27225

Chatzopoulos, G. (2021). Accelerating deformation seismicity patterns before the March 3, 2021 Thessaly strong earthquake, First results, Bull. Seismol. Soc. Gr., 58, 0, 87–104. https://doi.org/10.12681/bgsg.27155

Cochran, E. S., Y. G. Li and J. E. Vidale (2006). Anisotropy in the shallow crust observed around the San Andreas fault before and after the 2004 M 6.0 parkfield earthquake, Bull. Seismol. Soc. Am., 96, 4 B, 364–375, https://doi.org/10.1785/0120050804

Cochran, E. S., J. E. Vidale and Y. G. Li (2003). Near-fault anisotropy following the Hector Mine earthquake, J. Geophys. Res.: Solid Earth, 108, B9. https://doi.org/10.1029/2002jb002352

Crampin, S. (2001). Developing stress-monitoring sites using cross-hole seismology to stress-forecast the times and magnitudes of future earthquakes, Tectonophysics, 338, 3–4, 233–245, https://doi.org/10.1016/S0040-1951(01)00079-8

Crampin, S. and B. K. Atkinson (1985). Microcracks in the Earth's crust. First Break, 3, 3. https://doi.org/10.3997/1365-2397.1985005

Crampin, S. and S. Zatsepin (1997). Modelling the compliance of crustal rock—II. Response to temporal changes before earthquakes, Geophys. J. Int., 129, 495–506. https://doi.org/10.1111/j.1365-246X.1997.tb04489.x

Crampin, S. and Y. Gao (2018). Evidence supporting New Geophysics, Earth Planet. Ph., 2018, Vol. 2, Issue 3, Pages: 173-188, 2(3), 173–188. https://doi.org/10.26464/EPP2018018

Crampin, S., T. Volti and R. Stefánsson (1999). A successfully stress-forecast earthquake, Geophys. J. Int., 138(1), F1–F5. https://doi.org/10.1046/j.1365-246x.1999.00891.x

Crampin, S., Y. Gao and S. Peacock (2008). Stress-forecasting (not predicting) earthquakes: A paradigm shift, Geology, 36(5), 427. https://doi.org/10.1130/G24643A.1

Crampin, S., Y. Gao and A. de Santis (2013). A few earthquake conundrums resolved, J. Asian. Earth. Sci., 62, 501–509. https://doi.org/10.1016/j.jseaes.2012.10.036

Crampin, S., Y. Gao and J. Bukits (2015). A review of retrospective stress-forecasts of earthquakes and eruptions, Phys. Earth Planet. Inter., 245, 76–87. https://doi.org/10.1016/j.pepi.2015.05.008

Crotwell, H. P., T. J. Owens and J. Ritsema (1999). The TauP Toolkit: Flexible Seismic Travel-time and Ray-path Utilities, Seismol. Res. Lett., 70(2), 154–160. https://doi.org/10.1785/gssrl.70.2.154

De Novellis, V., D. Reale, G. M. Adinolfi, E. Sansosti and V. Convertito (2021). Geodetic model of the march 2021 Thessaly seismic sequence inferred from seismological and InSAR data, Remote Sens. 13, 3410. https://doi.org/10.3390/rs13173410

del Pezzo, E., F. Bianco, S. Petrosino and G. Saccorotti (2004). Changes in the coda decay rate and shear-wave splitting parameters associated with seismic swarms at Mt. Vesuvius, Italy, Bull. Seismol. Soc. Am., 94, 2, 439–452, https://doi.org/10.1785/0120030141

Evangelidis, C. P. (2017). Seismic anisotropy in the Hellenic subduction zone: Effects of slab segmentation and subslab mantle flow, Earth Planet. Sci. Lett., 480, 97–106, https://doi.org/10.1016/j.epsl.2017.10.003

Evangelidis, C. P., N. Triantafyllis, M. Samios, K. Boukouras, K. Kontakos, O. J. Ktenidou, I. Fountoulakis, I Kalogeras, N. S. Melis, O. Galanis, C. B. Papazachos,P. Hatzidimitriou,E. Scordilis, E. Sokos,P. Paraskevopoulos, A. Serpetsidaki, G. Kaviris, V. Kapetanidis, P. Papadimitriou, N. Voulgaris, I. Kassaras, G. Chatzopoulos, I. Makris, F. Vallianatos, K. Kostantinidou, C. Papaioannou, N. Theodoulidis, B. Margaris, S. Pilidou, I. Dimitriadis, P. Iosif, M. Manakou, Z. Roumelioti, K. Pitilakis, E. Riga, G. Drakatos, A. Kiratzi and G. A. Tselentis (2021). Seismic Waveform Data from Greece and Cyprus: Integration, Archival, and Open Access, Seismol. Res. Lett., 92, 3, 1672–1684. https://doi.org/10.1785/0220200408

Evans, R. (1984). Effects of the Free Surface on Shear Wave Trains, Geoph. J. Roy. Astr. Soc., 76, 165–172.

Ganas, A. (2022). NOAFAULTS KMZ layer Version 4.0. https://doi.org/10.5281/ZENODO.6326260

Ganas, A., I. A. Oikonomou and C. Tsimi (2017). NOAfaults: a digital database for active faults in Greece. Bull. Geol. Soc. Greece, 47, 2, 518, https://doi.org/10.12681/bgsg.11079

Ganas, A., S. Valkaniotis, P. Briole, A. Serpetsidaki, V. Kapetanidis, I. Karasante, I. Kassaras, G. Papathanassiou, I. Karamitros, V. Tsironi, P. Elias, V. Sarhosis, A. Karakonstantis, E. Konstantakopoulou, P. Papadimitriou and E. Sokos (2021). Domino-style earthquakes along blind normal faults in Northern Thessaly (Greece): kinematic evidence from field observations, seismology, SAR interferometry and GNSS, Bull. Geol. Soc. Greece, 58, 37, https://doi.org/10.12681/bgsg.27102

Gao, Y. and S. Crampin (2006). A stress-forecast earthquake (with hindsight), where migration of source earthquakes causes anomalies in shear-wave polarisations, Tectonophysics, 426, 3–4, 253–262, https://doi.org/10.1016/j.tecto.2006.07.013

Gao Y, A. Chen Y. Shi Z. Zhang and L. Liu (2019) Preliminary analysis of crustal shear-wave splitting in the Sanjiang lateral collision zone of the southeast margin of the Tibetan Plateau and its tectonic implications, Geophys. Prospect., 67, 2432–2449, https://doi.org/10.1111/1365-2478.12870

Galanakis, D., S. Sboras, G. Konstantopoulou and M. Xenakis (2021). Neogene-Quaternary tectonic regime and macroseismic observations in the Tyrnavos-Elassona broader epicentral area of the March 2021, intense earthquake sequence, Bull. Geol. Soc. Greece, 58, 200, https://doi.org/10.12681/bgsg.27196

Hess, H. H. (1964). Seismic Anisotropy of the Uppermost Mantle under Oceans, Nature, 203, 4945, 629–631, https://doi.org/10.1038/203629a0

Hunter, J. D. (2007). Matplotlib: A 2D Graphics Environment, Comput. Sci. Eng., 9, 3, 90–95, https://doi.org/10.1109/MCSE.2007.55

Ismaïl, W. ben and D. Mainprice (1998). An olivine fabric database: An overview of upper mantle fabrics and seismic anisotropy, Tectonophysics, 296, 1–2, 145–157, https://doi.org/10.1016/S0040-1951(98)00141-3

Kaneshima, S. (1990). Origin of crustal anisotropy: Shear Wave splitting studies in Japan, J. Geophys. Res., 95, 11121, https://doi.org/10.1029/JB095iB07p11121

Kaneshima, S., M. Ando and S. Kimura (1988). Evidence from shear-wave splitting for the restriction of seismic anisotropy to the upper crust, Nature, 335, 6191, 627–629, https://doi.org/10.1038/335627a0

Kapetanidis, V. and I. Kassaras (2019). Contemporary crustal stress of the Greek region deduced from earthquake focal mechanisms, J. Geodyn., 123, 55–82, https://doi.org/10.1016/j.jog.2018.11.004

Karakostas, V., C. Papazachos, E. Papadimitriou, M. Foumelis, A. Kiratzi, C. Pikridas, A. Kostoglou, C. Kkallas, N. Chatzis, S. Bitharis, A. Chatzipetros, A. Fotiou, C. Ventouzi, E. Karagianni, P. Bonatis, C. Kourouklas, P. Paradisopoulou, E. Scordilis, D. Vamvakaris, I. Grendas, D. Kementzetzidou, A. Panou, G. Karakaisis, I. Karagianni, P. Hatzidimitriou and O. Galanis (2021). The March 2021 Tyrnavos, central Greece, doublet (Mw6.3 and Mw6.0): Aftershock relocation, faulting details, coseismic slip and deformation, Bull. Geol. Soc. Greece, 58, 131, https://doi.org/10.12681/bgsg.27237

Kassaras, I., V. Kapetanidis, A. Ganas, A. Karakonstantis, P. Papadimitriou, G. Kaviris, V. Kouskouna and N. Voulgaris (2022). Seismotectonic analysis of the 2021 Damasi-Tyrnavos (Thessaly, Central Greece) earthquake sequence and implications on the stress field rotations, J. Geodyn., 150, https://doi.org/10.1016/J.JOG.2022.101898

Kaviris, G., 2003. Study of Seismic Source Properties of the Eastern Gulf of Corinth, Ph D. Thesis, Geophysics-Geothermics Department, Faculty of Geology, University of Athens, Greece, 2003 (in Greek).

Kaviris, G., P. Papadimitriou, P. Kravvariti, V. Kapetanidis, A. Karakonstantis, N. Voulgaris and K. Makropoulos (2015). A detailed seismic anisotropy study during the 2011-2012 unrest period in the Santorini Volcanic Complex, Phys. Earth Planet. Inter., 238, 51–88, https://doi.org/10.1016/j.pepi.2014.11.002

Kaviris, G., I. Spingos, V. Kapetanidis, P. Papadimitriou, N. Voulgaris, N. and K. Makropoulos (2017). Upper crust seismic anisotropy study and temporal variations of shear-wave splitting parameters in the western Gulf of Corinth (Greece) during 2013, Phys. Earth Planet. Inter., 269, https://doi.org/10.1016/j.pepi.2017.06.006

Kaviris, G., I. Fountoulakis, I. Spingos, C. Millas and P. Papadimitriou (2018a). Mantle dynamics beneath Greece from SKS and PKS seismic anisotropy study, Acta Geophys., 2008, https://doi.org/10.1007/s11600-018-0225-z

Kaviris, G., I. Spingos, C. Millas, V. Kapetanidis, I. Fountoulakis, P. Papadimitriou, N. Voulgaris and G. Drakatos (2018b). Effects of the January 2018 seismic sequence on shear-wave splitting in the upper crust of Marathon (NE Attica, Greece), Phys. Earth Planet. Inter., 285, 45–58, https://doi.org/10.1016/j.pepi.2018.10.007

Kaviris, G., C. Millas, I. Spingos, V. Kapetanidis, I. Fountoulakis, P. Papadimitriou, N. Voulgaris and K. Makropoulos (2018c). Observations of shear-wave splitting parameters in the Western Gulf of Corinth focusing on the 2014 Mw = 5.0 earthquake, Phys. Earth Planet. Inter., 282, 60–76, https://doi.org/10.1016/j.pepi.2018.07.005

Kaviris, G., I. Spingos, V. Karakostas, E. Papadimitriou, E. and T. Tsapanos (2020). Shear-wave splitting properties of the upper crust, during the 2013–2014 seismic crisis, in the CO2-rich field of Florina Basin, Greece, Phys. Earth Planet. Inter., 303, 106503, https://doi.org/10.1016/j.pepi.2020.106503

Kaviris, G., I. Spingos, V. Kapetanidis, P. Papadimitriou and N. Voulgaris (2021). On the origin of upper crustal shear-wave anisotropy at Samos Island, Greece. Acta Geophysica, 69, 3, 1051–1064, https://doi.org/10.1007/s11600-021-00598-2

Koukouvelas, I.K., K.G. Nikolakopoulos, A. Kyriou, R. Caputo, A. Belesis, V. Zygouri, S. Verroios, D. Apostolopoulos and I. Tsentzos (2021). The March 2021 Damasi Earthquake Sequence, Central Greece: Reactivation Evidence across the Westward Propagating Tyrnavos Graben, Geosciences 11, 328, https://doi.org/10.3390/geosciences11080328

Kouli, M., S. Peleli, V. Saltas, J. P. Makris and F. Vallianatos (2021). Robust Satellite Techniques for mapping thermal anomalies possibly related to seismic activity of March 2021, Thessaly Earthquakes, Bull. Geol. Soc. Greece 58, 105, https://doi.org/10.12681/bgsg.27058

Krischer, L., T. Megies, R. Barsch, M. Beyreuther, T. Lecocq, C. Caudron and J. Wassermann (2015). ObsPy: A bridge for seismology into the scientific Python ecosystem, Comput. Sci. Discov., 8, 1, 0–17, https://doi.org/10.1088/1749-4699/8/1/014003

Lazos, I., S. Sboras, K. Chousianitis, S. Bitharis, E. Mouzakiotis, V. Karastathis, C. Pikridas, A. Fotiou and D. Galanakis (2021). Crustal deformation analysis of Thessaly (Central Greece) before the march 2021 earthquake sequence near Elassona-Tyrnavos (northern Thessaly), Acta Geodyn. Geomater., 18, 379–385, https://doi.org/10.13168/AGG.2021.0026

Lekkas, E., K. Agorastos, S. Mavroulis, C. Kranis, E. Skourtsos, P. Carydis, M. Gogou, K. N. Katsetsiadou, G. Papadopoulos, I. Triantafyllou, A. Agalos, S. Moraitis, E. Stamati, D. Psarris, G. Kaviris, V. Kapetanidis, P. Papadimitriou, A. Karakonstantis, I. Spingos, V. Kouskouna, I. Kassaras, K. Pavlou, N. Voulgaris, M. Mavrouli, S. Pavlides, A. Chatzipetros, S. Sboras, E. Kremastas, A. Chatziioannou, A. Kiratzi, C. Papazachos, N. Chatzis, V. Karakostas, E. Papadimitriou, I. Koukouvelas, K. Nikolakopoulos, A. Kyriou, D. Apostolopoulos, V. Zygouri, S. Verroios, A. Belesis, I. Tsentzos, P. Krassakis, K. Lymperopoulos, A. Karavias, D. Bafi, T. Gatsios, M. Karatzia, I. Gkougkoustamos, T. Falaras, I. Parcharidis, G. Papathanassiou, C. P. Evangelidis, V. Karastathis, G. A. Tselentis, A. Ganas, V. Tsironi, I. Karasante, S. Valkaniotis, D. Galanakis, G. Kostantopoulou, N. Papadopoulos, A. Kourou, M. Manousaki and T. Thoma (2021). The early March 2021 Thessaly earthquake sequence. Newsletter of Environ. Disaster Crises Management Strategies, 22, March 2021, p. 195 (ISSN 2653-9454).

Li, Z. and Z. Peng (2017). Stress- and Structure-Induced Anisotropy in Southern California From Two Decades of Shear Wave Splitting Measurements, Geophys. Res. Lett., 44, 19, 9607-9614, https://doi.org/10.1002/2017GL075163

Li, Z., H. Zhang and Z. Peng (2014). Structure-controlled seismic anisotropy along the Karadere-Düzce branch of the North Anatolian Fault revealed by shear-wave splitting tomography. Earth and Planet. Sci. Lett., 391, 319-326, https://doi.org/10.1016/j.epsl.2014.01.046

Makropoulos, K., G. Kaviris and V. Kouskouna (2012). An updated and extended earthquake catalogue for Greece and adjacent areas since 1900. Nat. Hazards Earth Syst. Sci., 12, 5, 1425-1430, https://doi.org/10.5194/nhess-12-1425-2012

Mavroulis, S., M. Mavrouli, P. Carydis, K. Agorastos and E. Lekkas (2021). The March 2021 Thessaly earthquakes and their impact through the prism of a multi-hazard approach in disaster management, Bull. Geol. Soc. Greece, 58, 1, https://doi.org/10.12681/bgsg.26852

Michas, G., K. Pavlou, S.E. Avgerinou, E.A. Anyfadi and F. Vallianatos (2022). Aftershock patterns of the 2021 Mw 6.3 Northern Thessaly (Greece) earthquake, J. Seismol. 26, 201-225, https://doi.org/10.1007/s10950-021-10070-9

National Observatory Of Athens, Institute of Geodynamics (1997). National Observatory of Athens Seismic Network, International Federation of Digital Seismograph Networks, https://doi.org/10.7914/SN/HL.

Nolte, K. A., G. P. Tsoflias, T. S. Bidgoli and W. L. Watney (2017). Shear-wave anisotropy reveals pore fluid pressure-induced seismicity in the U.S. midcontinent, Sci. Adv., 3, 12, e1700443, https://doi.org/10.1126/sciadv.1700443

Ortega-Romo, A. D., J. I. Walter, X. Chen and B. M. Carpenter (2021). Spatially Distinct Tectonic Zones across Oklahoma Inferred from Shear-Wave Splitting, Seismol. Res. Lett., 92, 4, 2551-2561, https://doi.org/10.1785/0220200237

Papadimitriou, E. and V. Karakostas (2003). Episodic occurrence of strong (Mw ≥ 6.2) earthquakes in Thessalia area (central Greece). Earth Planetary Sc. Letters, 215, 395-409.

Papadimitriou, P., G. Kaviris and K. Makropoulos (1999). Evidence of shear-wave splitting in the eastern Corinthian Gulf (Greece), Earth Planet. Inter., 114, 1-2, 3-13.

Papadopoulos, G. A., A. Agalos, A. Karavias, I. Triantafyllou, I. Parcharidis and E. Lekkas (2021). Seismic and Geodetic Imaging (DInSAR) Investigation of the March 2021 Strong Earthquake Sequence in Thessaly, Central Greece, Geosciences, 11, 8, 311, https://doi.org/10.3390/GEOSCIENCES11080311

Papathanassiou, G., S. Valkaniotis, A. Ganas, A. Stampolidis, D. Rapti and R. Caputo (2022). Floodplain evolution and its influence on liquefaction clustering: The case study of March 2021 Thessaly, Greece, seismic sequence, Eng. Geol. 298, 106542, https://doi.org/10.1016/j.enggeo.2022.106542

Papazachos, V. and K. Papazachou (2003). The earthquakes of Greece. Ziti Publications Co.

Pastori, M., P. Baccheschi and L. Margheriti (2019). Shear Wave Splitting Evidence and Relations With Stress Field and Major Faults From the Amatrice-Visso-Norcia Seismic Sequence, Tectonics, 38, 9, 3351-3372, https://doi.org/10.1029/2018TC005478

Pavlides, S.B. and S.P. Sboras (2021). Recent earthquake activity of March 2021 in northern Thessaly unlocks new scepticism on faults, Turkish J. Earth Sci. 30, 851-861, https://doi.org/10.3906/YER-2110-6

Peng, Z. and Y. Ben-Zion (2004). Systematic analysis of crustal anisotropy along the Karadere-Düzce branch of the North Anatolian fault, Geophys. J. Int., 159, 1, 253-274, https://doi.org/10.1111/j.1365-246X.2004.02379.x

Polat, G., N. M. Ozel, S. Crampin, S. Ergintav and O. Tan (2012). Shear wave splitting as a proxy for stress forecast of the case of the 2006 Manyas-Kus Golu (Mb Combining double low line 5.3) earthquake, Nat. Hazards Earth Syst. Sci., 12, 4, 1073-1084, https://doi.org/10.5194/nhess-12-1073-2012

Savage, M. K., A. Wessel, N. A. Teanby and A. W. Hurst (2010). Automatic measurement of shear wave splitting and applications to time varying anisotropy at Mount Ruapehu volcano, New Zealand, J. Geophys. Res. Solid Earth, 115, 12. https://doi.org/10.1029/2010JB007722

Seher, T. and I. G. Main (2004). A statistical evaluation of a "stress-forecast" earthquake, Geophys. J. Int., 157, 1, 187-193. https://doi.org/10.1111/j.1365-246X.2004.02186.x

Silver, P. G. and W. W. Chan (1991). Shear Wave Splitting and Sub continental Mantle Deformation, J. Geophys. Res., 96, 429-454, https://doi.org/10.1029/91JB00899

Song, C.Z.L., C. Yu and G. Meldebekova (2022). Normal Fault Slips of the March 2021 Greece Earthquake Sequence from InSAR Observations, J. Geod. and Geoinf. Sci. 5, 50, https://doi.org/10.11947/j.JGGS.2022.0106

Spingos, I., G. Kaviris, C. Millas, P. Papadimitriou and N. Voulgaris (2020). Pytheas: An open-source software solution for local shear-wave splitting studies, Comput. and Geosci., 134, 104346, https://doi.org/10.1016/j.cageo.2019.104346

Spingos, I., F. Vallianatos and G. Kaviris (2021). The scaling of PGA with IV2p and its potential for Earthquake Early Warning in Thessaly (Central Greece), Bull. Geol. Soc. Greece, 58, 0, 179, https://doi.org/10.12681/bgsg.27062

Stucchi, M., A. Rovida, A. A. Gomez Capera, a. a., Alexandre, P., Camelbeeck, T., Demircioglu, M. B., Gasperini, P., Kouskouna, V., Musson, R. M. W., Radulian, M., Sesetyan, K., Vilanova, S., Baumont, D., Bungum, H., Fäh, D., Lenhardt, W., Makropoulos, K., Martinez Solares, J. M., Scotti, O., M. Živčić, P. Albini, J. Batllo, C. Papaioannou, R. Tatevossian, M. Locati, C. Meletti, D. Viganò and D. Giardini (2013). The SHARE European Earthquake Catalogue (SHEEC) 1000-1899, J. Seismol., 17, 523-544, https://doi.org/10.1007/s10950-012-9335-2

Tai, L.-X., Y. Gao, K. F. Ma, E. T. Lee, Y. T. Shi and H. I. Lin (2011). Crustal Anisotropy in North Taiwan from Shear-Wave Splitting, Chin. J. Geophys., 54, 5, 627-636, https://doi.org/10.1002/cjg2.1646

Teanby, N., J. M. Kendall and M. van der Baan (2004). Automation of shear-wave splitting measurements using cluster analysis, Bull. Seismol. Soc. Am., 94, 2, 453-463, https://doi.org/10.1785/0120030123

Tolomei, C., R. Caputo, M. Polcari, N. A. Famiglietti, M. Maggini and S. Stramondo (2021). The Use of Interferometric Synthetic Aperture Radar for Isolating the Contribution of Major Shocks: The Case of the March 2021 Thessaly, Greece, Seismic Sequence, Geosciences 11, 191, https://doi.org/10.3390/geosciences11050191

Tommasi, A., B. Tikoff and A. Vauchez (1999). Upper mantle tectonics: three-dimensional deformation, olivine crystallographic fabrics and seismic properties, Earth and Planet. Sci. Lett., 168, 1-2, 173-186, https://doi.org/10.1016/S0012-821X(99)00046-1

Uieda, L., D. Tian, W. J. Leong, L. Toney, W. Schlitzer, J. Yao, M. Grund, M. Jones, K. Materna, T. Newton, M. Ziebarth and P. Wessel (2021). PyGMT: A Python interface for the Generic Mapping Tools, https://doi.org/10.5281/ZENODO.4592991

University of Patras, Geology Department (2000). PSLNET, permanent seismic network operated by the University of Patras, Greece, International Federation of Digital Seismograph Networks, https://doi.org/10.7914/SN/HP.

Valcke, S. L. A., M. Casey, G. E. Lloyd, J. M. Kendall and Q. K. Fisher (2006). Lattice preferred orientation and seismic anisotropy in sedimentary rocks, Geophys. J. Int., 166, 2, 652-666, https://doi.org/10.1111/j.1365-246X.2006.02987.x

Valkaniotis, S., G. Papathanassiou, A. Ganas, E. Kremastas and R. Caputo (2021). Preliminary report of liquefaction phenomena triggered by the March 2021 earthquakes in Central Thessaly, Greece, Zenodo. http://doi.org/10.5281/zenodo.4608365

Walsh, E., R. Arnold and M. K. Savage (2013). Silver and Chan revisited, J. Geophys. Res. Solid Earth, 118, 10, 5500-5515. https://doi.org/10.1002/jgrb.50386

Wessel, P., J. F. Luis, L. Uieda, R. Scharroo, F. Wobbe, W. H. F. Smith and D. Tian (2019). The Generic Mapping Tools Version 6, Geochem. Geophys. Geosystems, 20, 11, 5556-5564, https://doi.org/10.1029/2019GC008515

Wüstefeld, A. and G. Bokelmann (2007). Null detection in shear-wave splitting measurements, Bull. Seismol. Soc. Am., 97, 4, 1204-1211. https://doi.org/10.1785/0120060190

Yang, J., C. Xu, Y. Wen and G. Xu (2022). Complex Coseismic and Postseismic Faulting During the 2021 Northern Thessaly (Greece) Earthquake Sequence Illuminated by InSAR Observations, Geophys. Res. Lett. 49, https://doi.org/10.1029/2022GL098545

Zatsepin, S. and S. Crampin (1997). Modelling the compliance of crustal rock—I. Response of shear-wave splitting to differential stress, Geophys. J. Int., 129, 477-494, https://doi.org/10.1111/j.1365-246X.1997.tb04488.x

Zinke, J. C. and M. D. Zoback (2000). Structure-related and stress-induced shear-wave velocity anisotropy: Observations from microearthquakes near the Calaveras Fault in Central California, Bull. Seismol. Soc. Am., 90, 5, 1305-1312, https://doi.org/10.1785/0119990099

***CORRESPONDING AUTHOR: George KAVIRIS**,
Section of Geophysics – Geothermics, Department of Geology and Geoenvironment,
National and Kapodistrian University of Athens, Athens, Greece
e-mail: gkaviris@geol.uoa.gr